A deep neural network for achieving spectrally consistent and seamless infrared radiance measurements across geostationary satellite domains

Benjamin Scarino*[a], David R. Doelling[a], William L. Smith[a], Conor Haney[b], Rajendra Bhatt[a], Arun Gopalan[b], and Prathana Khakurel[b]
[a]NASA Langley Research Center, 21 Langley Blvd MS 420, Hampton, VA 23681 USA
[b]Analytical Mechanics Associates, 21 Enterprise Pkwy, Hampton, VA 23666 USA

ABSTRACT

The NASA Clouds and the Earth's Radiant Energy System (CERES) project provides the scientific community with observed top-of-atmosphere (TOA) shortwave and longwave fluxes for climate monitoring and climate model validation. To achieve this goal, CERES relies on TOA broadband fluxes derived from geostationary satellite (GEO) imagery to account for the diurnal flux variations between the CERES observation intervals. Consistent global flux derivation depends on accurate and consistent cloud retrievals. Scene-dependent spectral measurement inconsistency of the instruments that make up the contiguous ring of GEO observations (GEO-Ring), as well as limb darkening effects, can cause discontinuities in derived cloud properties and radiative fluxes at the boundaries of adjacent imager domains. Although the algorithms utilize radiative transfer models to account for instrument-band-dependent atmospheric correction and viewing zenith angle (VZA) dependency, small discontinuities may persist due to uncertainties inherent to the multiple imager-specific algorithms. Furthermore, while hyperspectral-instrument-based spectral band adjustment factors may effectively account for spectrally induced bias, they are less effective at reducing variance owed to the specific composition of the viewed scene, which is challenging to robustly characterize. As such, this article highlights the use of a deep neural network (DNN) to resolve spectral- and VZA-induced biases between GEO-Ring imagers. The DNN uses available infrared (IR) channels from the GEO instruments, along with viewing and solar illumination geometry, to estimate homogenized, VIIRS-like IR radiances for use in the GEO cloud algorithm. This approach is effective at mitigating scene-dependent spectral variance and VZA dependency, resulting in consistent radiance measurements across the GEO-Ring, thereby leading toward a more seamless global cloud assessment.

1. INTRODUCTION

The NASA Clouds and the Earth's Radiant Energy System (CERES) project provides a continuous global top-of-atmosphere (TOA) shortwave and longwave flux observation record for the purpose of detecting decadal changes in Earth's energy balance. The CERES instruments operate onboard Sun-synchronous satellites with consistent local equator crossing times, and geostationary satellite (GEO) imagers are employed to derive broadband fluxes for determining the diurnal flux variations at times between the Sun-synchronous CERES flux observations. The continuous temporal monitoring centered at a fixed GEO equatorial longitude position is the primary benefit of the CERES GEO synoptic 1° gridded cloud and flux data product[2]. For the Edition 4 (Ed4) product, 1-hourly imager radiances are obtained from the contiguous ring of 5 GEO positions (GEO-Ring) beginning in March 2000. For both historical and forward processing, the imager radiances are used to retrieve cloud and radiative properties at the pixel level, which are aggregated monthly for each processing hour to produce a global 1° gridded product of cloud and flux data. Therefore, it is advantageous that the pixel-level radiances from each satellite in the GEO-Ring, which the cloud/flux products are derived from, are radiometrically and spectrally consistent with one another.

Aside from the visible channel (VIS; ~0.65 µm), the GEO Ed4 forward-processing algorithms rely mainly on the ~3.9-, ~11, ~8.7-, and ~12-µm bands (T39, T11, T87, and T12, respectively) for cloud property retrievals. Although VIS is the primary channel used to estimate daytime cloud optical depth (COD), T39 primarily for particle size, T11 for temperature, and T87 and T12 for phase selection, all contribute to the cloud mask and the interpretation of COD[3]. It is important that the retrievals are consistent, not only across the imager records but also between concurrent imagers that make up the GEO-Ring. Therefore, it is important that imager band radiances are well calibrated. Multiple VIS-band inter-calibration and stability monitoring approaches are employed to ensure consistent observations across the 23 GEOs

Keywords: deep learning, machine learning, neural network, calibration, homogenization, GEO-Ring, VIIRS

*benjamin.r.scarino@nasa.gov

used in CERES, but infrared (IR) bands are assumed to be stable and no adjustments to the IR calibrations are employed[4,5]. This assumption is owed to the presence of blackbody references onboard each satellite that ensure the temporal stability and accuracy of the IR calibrations[6,7]. Although these onboard calibration mechanisms lend confidence to the IR radiometric accuracy of the different imagers, they do not account for the relative spectral and retrieval bias considerations of the calibration sequence[8]. That is, effects like measurement differences owed to the spectral disparity of common channels across different imagers and the viewing zenith angle (VZA) dependency of limb darkening must still be corrected[9,10]. In the GEO Ed4 algorithm, these effects were only partially accounted for with correlated-k-distribution radiative transfer model (RTM) schemes for atmospheric transmittance and limb darkening models[11,12,13].

We address spectral discontinuity and limb darkening effects with a newly developed, machine-learning-based absolute calibration method for producing homogenized GEO IR radiances. Distinct from common statistical methods, this deep neural network (DNN) approach ties GEO IR channel radiances, VZA, solar zenith angle (SZA), and relative azimuth angle (RAA) to National Oceanic and Atmospheric Administration (NOAA-20) Visible Infrared Imaging Radiometer Suite (VIIRS) reference channels[4,5,14]. We use multiple GEO IR channels as predictors for a coincident VIIRS reference channel, thereby providing information about the spectral characteristics of the scene being observed by both instruments. The goal is to achieve a more robust, scene-dependent spectral band adjustment than can be achieved through more traditional RTM or hyperspectral convolutional approaches, while simultaneously accounting for VZA dependency and any lingering radiometric biases[15]. With this method, we aim to produce a more seamless global cloud assessment through homogenization of GEO-Ring radiance measurements.

2. METHODOLOGY

2.1 Dataset Curation

The GEO IR spectral calibration DNN method relies on collocated NOAA-20 VIIRS and GEO IR radiances. The collocated VIIRS and GEO radiances, evaluated as brightness temperatures (BTs), are averaged to a common 0.25º grid that spans the globe between 60º N and 60º S, matched within a 15-min time difference at all allowable VZA, SZA, and RAA configurations. The matched GEOs comprise those being used currently for CERES GEO broadband flux derivation, consisting of Geostationary Operational Environmental Satellite (GOES) 18 (G18), GOES-16 (G16), Meteosat-10 (MET10), Meteosat-9 (MET9), and Himawari-9 (HIM9). The saved spectral channels include bands M12 (~3.9 µm), M14 (~8.5 µm), M15 (~11 µm), and M16 (~12 µm) from VIIRS, along with the GOES, Meteosat, and Himawari BT channels most closely corresponding to the T39, ~6.7 µm, (T67), T87, T11, T12, and ~13 µm (T13) bands. A full year of gridded VIIRS and GEO radiance and angular data, collected between 2023 and 2024 April, constitutes the dataset curated for DNN development.

2.2 Deep Neural Network Setup

Training, validation, and testing datasets for two distinct DNN applications are subsetted from the curated dataset. In the first application, the DNN is trained to predict VIIRS-like radiances as viewed from VIIRS at nadir, and in the second application the DNN predicts ray-matched VIIRS-like radiances. The former model is designed to achieve seamless radiance values across all GEO domains by accounting for both spectral biases and limb darkening, whereas the latter model is meant to only account for spectral biases, with the assumption that a nadir-equivalent view at all GEO pixels is not suitable for all scientific applications (e.g., the GEO cloud algorithm). In either case, the curated dataset is further filtered for homogeneity consideration such that each 0.25º grid box radiance average must have been computed from at least 3 VIIRS and GEO samples with T39 and T11 standard deviations less than 3 K. For the VIIRS at-nadir application, VIIRS samples are limited to those with VZA less than 5º. For the VIIRS ray-matched application, VIIRS and GEO SZA, VZA, and RAA must match one another within 15º (note that due to the 15-min maximum time difference, SZA always matches within ~3.5º). In both cases, the filtered data are assigned, randomly by whole days, to training (80%), validation (15%), and testing (5%) sets. Across all GEOs, the *at-nadir* DNN application is, on average, based on 885,134 training, 163,914 validation, and 57,332 testing samples. For the *ray-matched* DNN application, the split is 980,599 training, 178,491 validation, and 59,853 testing.

All DNNs use the same predictors, consisting of the T39, T67, T87, T11, T12, T13, SZA, VZA, and RAA of whichever GEO is being adjusted. A separate DNN is trained for each GEO to produce homogenized, VIIRS-like T39, T87, T11, and T12 BTs. The same architecture is used for all DNNs, containing 10 hidden layers with 30 neurons per layer, rectified linear unit (ReLU) activation, trained with Adam Optimization across 128 minibatches at a learning rate of 0.001 that decays by 5% every 20 epochs for up to 400 epochs with early stopping[16,17,18,19,20,21]. All datasets are standardized based on the *z*-score of the training set before training and at application.

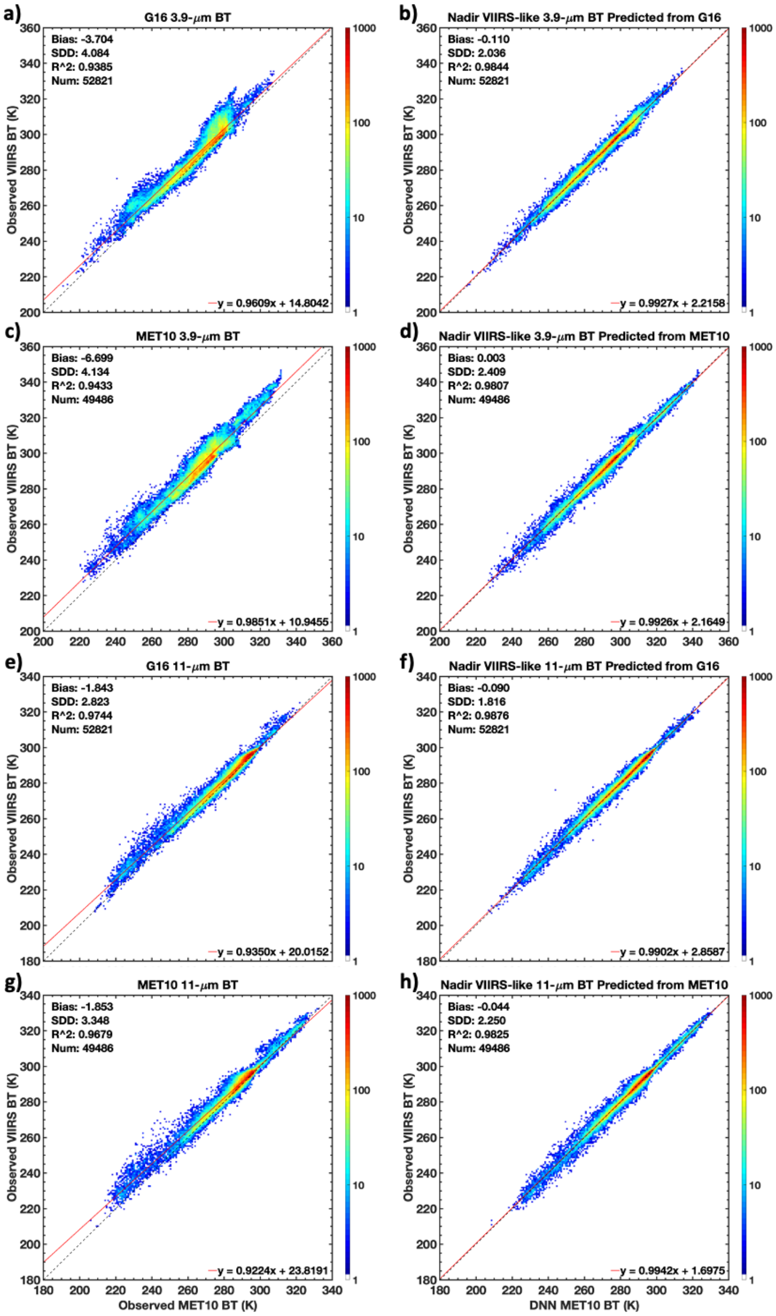

Figure 1. Testing set a,c,e,g) observed and b,d,f,h) *at-nadir* DNN-estimated G16 and MET10 T39 and T11 BTs relative to the respective at-nadir VIIRS reference channels. The large biases in the observed G16 and MET10 BTs are mainly owed to VZA dependency.

2.3 Validation Approaches

Beyond common DNN skill assessment methods, the seamless radiance *at-nadir* DNNs and the cloud algorithm application *ray-matched* DNNs are evaluated with distinct approaches. The at-nadir application is assessed by applying trained GEO-specific models to GEO imagery from a day found in the independent testing set – testing whether discontinuities in the BT imagery are reduced across the GEO domain boundaries. Furthermore, coincident VIIRS swaths (<5º VZA) are overlaid on the GEO testing set imagery to demonstrate the effectiveness of the nadir-VIIRS-like scaling. The ray-matched application is evaluated using the Ed4 GEO cloud algorithms for G16 and MET10, where MET10 is modified to use G16-based spectral assumptions about atmospheric transmittance and cloud masking[15]. In other words, MET10 is using G16-based RTM central wavelength and response definitions instead of its own definitions as is normally done[12,13]. The G16 and modified MET10 daytime-only cloud algorithms are processed for 11 days (21-31 July 2023), first using their native channel radiances, and again using T39, T87, T11, and T12 radiances that were adjusted to be VIIRS-like using the *ray-matched* DNNs. That is, G16 and MET10 radiances (either observed or VIIRS-like) are used to derive cloud products within a common algorithm that is based on G16 expectations. Note that visible channels are unaffected in this approach, meaning that both the G16 and MET10 algorithms always use their respective native reflectance channels and visible calibrations, regardless of whether MET10 uses G16 assumptions or whether the DNN has modified the T39, T87, T11, and T12 radiances[4,5].

3. RESULTS AND DISCUSSION

3.1 Deep Neural Network Predictive Skill

The skill of the DNNs is evaluated by monitoring the reduction in prediction vs. truth mean squared error (MSE) for the training and validation sets, and then checking the end-result MSE for the testing set. Alternatively, the single skill metric can be separated into terms of mean error and uncertainty to better parse the influence of the DNNs. Figure 1 shows the result of G16 and MET10 *at-nadir* DNN training for the T39 and T11 bands

Table I. Summary of testing set GEO observed and *at-nadir* DNN-estimated BT biases and SDDs relative to the VIIRS reference.

(K)		**GEO vs. VIIRS**		**DNN vs. VIIRS**	
		Bias	**SDD**	**Bias**	**SDD**
G18	**T39**	-3.86	4.08	-0.03	1.97
	T87	-2.19	2.63	-0.05	1.67
	T11	-1.90	2.70	-0.06	1.77
	T12	-2.93	2.67	0.07	1.76
G16	**T39**	-3.70	4.08	-0.11	2.04
	T87	-2.35	2.72	0.02	1.73
	T11	-1.84	2.82	-0.09	1.82
	T12	-2.93	2.81	0.00	1.80
MET10	**T39**	-6.70	4.13	0.00	2.41
	T87	-2.19	3.42	0.11	2.14
	T11	-1.85	3.35	-0.04	2.25
	T12	-2.17	3.42	-0.03	2.23
MET9	**T39**	-7.16	4.28	-0.01	2.33
	T87	-2.65	3.56	-0.06	2.16
	T11	-2.27	3.45	0.11	2.25
	T12	-2.65	3.52	0.05	2.24
HIM9	**T39**	-3.02	3.65	0.04	1.92
	T87	-2.77	3.06	0.01	1.75
	T11	-2.51	3.11	0.02	1.84
	T12	-3.88	3.18	0.03	1.82

applied to the respective testing sets, and the complete satellite band statistics are summarized in Table I. For all GEOs and bands, the DNNs are effective in reducing the mean difference (bias) and standard deviation of the difference (SDD) between the GEO BT and the VIIRS reference BT. The DNNs make reasonably accurate estimates of nadir-VIIRS-like BT along the full dynamic range of measurements, resulting in adjusted GEO biases near 0 K relative to at-nadir VIIRs, with SDD reduced by around 1–2 K, depending on the channel.

Note that the reason for the large, 2–6-K biases in observed GEO compared to VIIRS (Figs 1a,c,e,g) is almost entirely due to VZA dependency (except for the T39 band). That is, the DNNs are doing well to remove the GEO limb darkening effects. The dominance of the VZA-induced bias is demonstrated by comparing Fig. 1 with Fig. 2, the latter of which shows the same information except that the collocated GEO and VIIRS data are ray-matched instead of matched to nadir VIIRS. Here the average discrepancy is almost entirely owed to the spectral differences of the GEO and VIIRS channels, with a near 0-K bias for the T11 band (Figs. 2e,g) and bands T87 and T12 (not shown), even without the *ray-matched* DNN adjustments. With the DNN adjustments, there is little meaningful change in bias, but the SDD is reduced (Fig. 2f,h). Absolute bias even increases after the DNNs are applied for both G16 and MET10 (more so in the latter), and

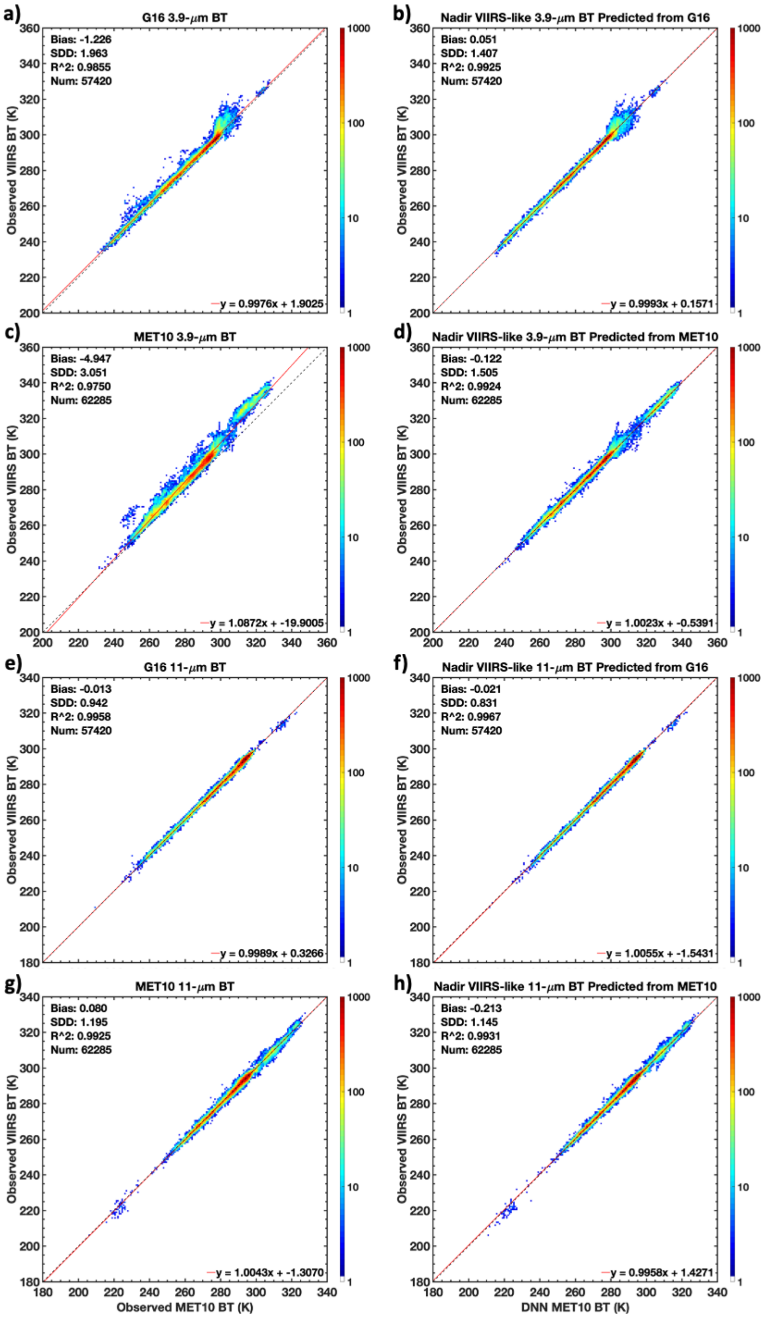

Figure 2. Testing set a,c,e,g) observed and b,d,f,h) *ray-matched* DNN-estimated G16 and MET10 T39 and T11 BTs relative to the respective ray-matched VIIRS reference channels.

the MET10 DNN seems to poorly characterize the absolute coldest BTs with estimates that are too warm (Fig. 2h), which could likely be mitigated with greater sampling of cold clouds. The fact that the variance improves despite small initial bias demonstrates the effectiveness of the DNNs in reducing scene-spectra-dependent uncertainty. This effectiveness is especially apparent for the T39 channel (Figs. 2a-d), for which spectral bias is still rather significant (particularly for MET10; Fig. 2c), and thus the impact of the DNN in characterizing T39 sensitivity is noticeable. That is, scene dependency of the spectral signature is amplified by T39 solar reflectance contribution and strong CO_2 absorption near 4.2 μm in the MET10 T39 band, which the DNNs are able to properly resolve.

Inference of scene composition, and its characterization, is accomplished through the inclusion of multiple imager bands in the DNN input predictor set. That is, a DNN using a single GEO band radiance predictor to estimate the corresponding VIIRS-like radiance, e.g., GEO T39 to predict VIIRS T39, is less skillful than a DNN using more band radiance predictors. Providing the DNN with more information about the spectral signature of the matched field-of-view enhances scene-spectra-dependent characterization and improves model skill. The significance of using multiple radiance predictors is demonstrated for both the *at-nadir* (top row) and *ray-matched* (bottom row) DNNs in Fig. 3. The adjusted radiances resulting from DNNs that use MET10 T39 to predict VIIRS T39 (in addition to SZA, VZA, and RAA) are a significant improvement (Figs. 3b,e) over the unadjusted colocations (Figs. 3a,d), but DNNs that include T39, T67, T87, T11, T12, and T13 are slightly more reliable (Figs. 3c,f). In the case of the *at-nadir* DNNs, for example, the model that uses 6-band radiance predictors (Fig. 3c) has ~0.4 K improved estimate uncertainty, with absolute bias reduced from ~0.2 K to near 0.0 K compared to the 1-band predictor model (Fig. 3b). What's most notable is the fact that the 6-band predictor result reveals much better characterization along the full dynamic range of estimates, with Fig. 3c cold and warm end estimates much more densely and linearly aligned along the major axis of matches compared to Fig. 3b. The enhancements the 6-band predictors offer for the *ray-matched* DNN (Fig. 3f) are more subtle compared to the *at-nadir* DNN, but nevertheless represent qualifiable and quantifiable improvements over the 1-band model (Fig. 3e). That is, although absolute bias remains roughly consistent, the SDD reduces by nearly 0.2 K while overall linearity improves.

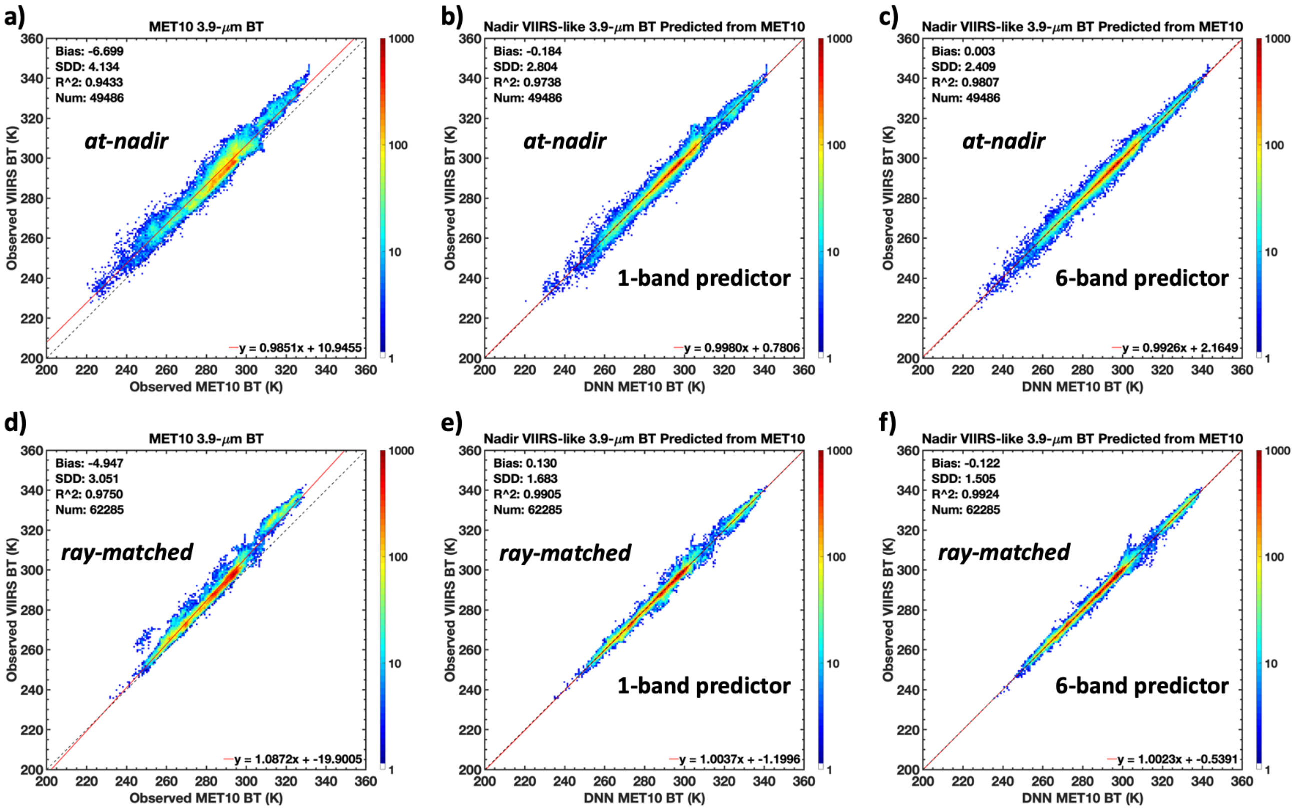

Figure 3. Testing set a,d) observed *at-nadir* (top) and *ray-matched* (bottom) DNN-estimated MET10 T39 relative to VIIRS T39 based on b,e) 1 band radiance predictor or c,f) 6 band radiance predictors.

3.2 Seamless Radiance Application

The effectiveness of the GEO-specific *at-nadir* DNNs in producing homogenized, nadir-VIIRS-like BTs is demonstrated with a testing set application study (Fig. 4). Here we see a view of GEO-Ring T39 (Figs. 4a,c) and T12 (Figs. 4b,d) 10' gridded radiances, both before (Figs. 4a,b) and after (Figs. 4c,d) application of the DNNs. Each panel also shows the solar terminator, with red indicating the daylit side. Without the DNNs, i.e., using the observed satellite radiances, discontinuities or "seams" are apparent at the inter-GEO boundaries. These are evident in Fig. 4 for T39 (Fig. 4a) and/or T12 (Fig. 4b) at 120º W, 30º W, 60º E, and 80º E for the G18/G16, G16/MET10, MET10/MET9, and MET9/HIM9 boundaries, respectively. After application of the DNNs, the seams almost entirely disappear, most evidently in T39 at 120º W and 60º E (Fig. 4c), and in T12 at 30ºW, 60º E, and 80º E. Note that similar behavior occurs for the HIM9/G18 boundary at 180º E, although this is not easily noticeable with the Fig. 4 map view.

One potential downside of the GEO adjustment to an at-nadir VIIRS lies in the fact that the Sun-synchronous orbit means that daytime applications will tend to correct toward an overhead-Sun Bidirectional Reflectance Distribution Function (BRDF) hot spot. This data feature may impact T39 applications given the significance of the solar reflectance contribution in this band. The effect is evident by the change in hot spot coverage between Fig. 4a and Fig. 4c. Figure 4a shows two distinct and small hot spot areas based on separate G18 and G16 viewing geometries, whereas Fig. 4c has an expansive single hot spot that is a result of the overhead, Sun-synchronous VIIRS assumption. Such an assumption may not be suitable for certain science application that rely on T39 radiances and that are sensitive to hot spot consideration. Regardless of hot-spot-related uncertainties, however, application of the DNNs reduces the total variance and standard deviation of zonally averaged BTs for all four estimated bands as summarized in Table II. As discussed in Section 3.1, this improved continuity around the GEO-Ring is largely owed to the removal of VZA dependency (see Figs. 1 and 2). As such, a similar mapped radiance comparison with, instead, the *ray-matched* DNN results would reveal a much more subtle change after DNN application, with seams persisting, as only smaller-magnitude spectral biases would be resolved (not shown).

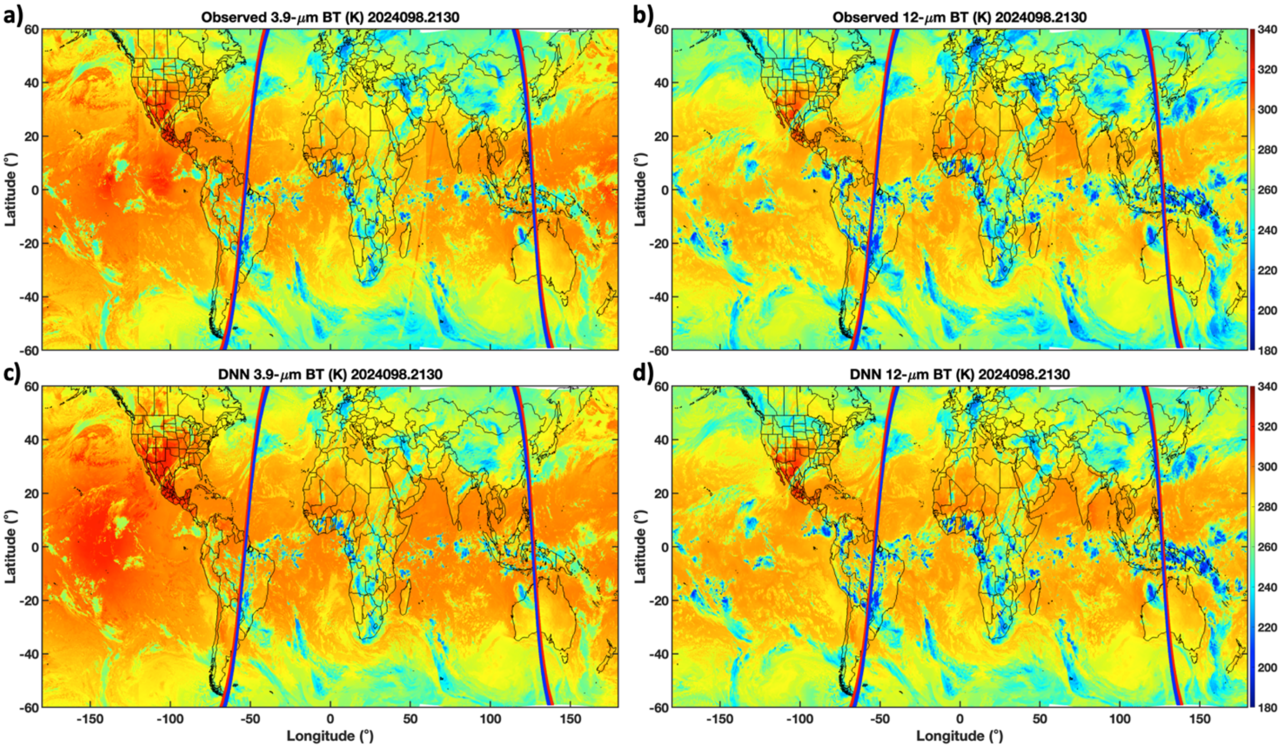

Figure 4. Testing set 7 April 2024, 21:30 UTC GEO-Ring of a,c) T39 and b,d) T12 radiances without (top) and with (bottom) application of GEO-specific *at-nadir* DNNs. The solar terminator is marked by the red and blue lines, where red indicates the daylit side. A coincident swath of parallax-corrected *at-nadir* VIIRS T39 or T12 radiance, for VZA less than 5º, is overlayed on each panel extending across the southern Indian Ocean, roughly from 60º S, 45º E to 60º N, 75º E, although only apparent on a) and b).

Table II. Percent reduction in total variance and standard deviation of zonal BT after applying *ray-matched* DNNs.

% Reduction	**T39**	**T87**	**T11**	**T12**
Total Variance	7.6	4.5	2.7	1.0
Standard Deviation	7.1	9.6	9.4	6.6

Beyond evaluating changes in inter-boundary continuity, the DNNs are evaluated in application by comparing with the at-nadir VIIRS reference. Because this case is taken from the testing set, any matched VIIRS swaths constitute an independent comparison. The parallax-corrected coincident VIIRS swath is evident in Figs. 4a,b as a narrow line of distinct T39 or T12 radiances extending roughly from 60º S, 45º E to 60º N, 75º E. This nighttime VIIRS swath is limited to VZAs less than 5º – the same criterion used for model truth. Although the same VIIRS swath is present in all four panels of Fig. 4, it is effectively made invisible by the GEO-to-nadir-VIIRS DNN adjustments (Figs. 4c,d). This blending is more easily examined in Fig 5, which is the same as Fig. 4, but focused closely on the VIIRS swath where it crosses the MET10/MET9 boundary. With this view, the distinction of the observed VIIRS T39 radiance compared to MET10 and MET9 T39 is rather clear (Fig. 5a), and that distinction virtually disappears after the DNNs are applied, thereby homogenizing the MET10 and MET9 radiances with VIIRS (Fig. 5c). The same behavior occurs for T12, although in this case the observed MET9 T12 seems to already be a close match to VIIRS T39, which is why the VIIRS swath is barely visible on the MET9 side of the boundary in Fig. 5b. This zoomed view, however, grants close examination of the change in T12 across both the MET10/MET9 and MET9/HIM9 boundaries, all of which are effectively homogenized with one another and VIIRS after the DNNs are applied (Fig. 5d). Note that small imperfections are evident in the T12 DNN application (Fig. 5d) in the form of 1) trace remnants of a seam at 60º E most

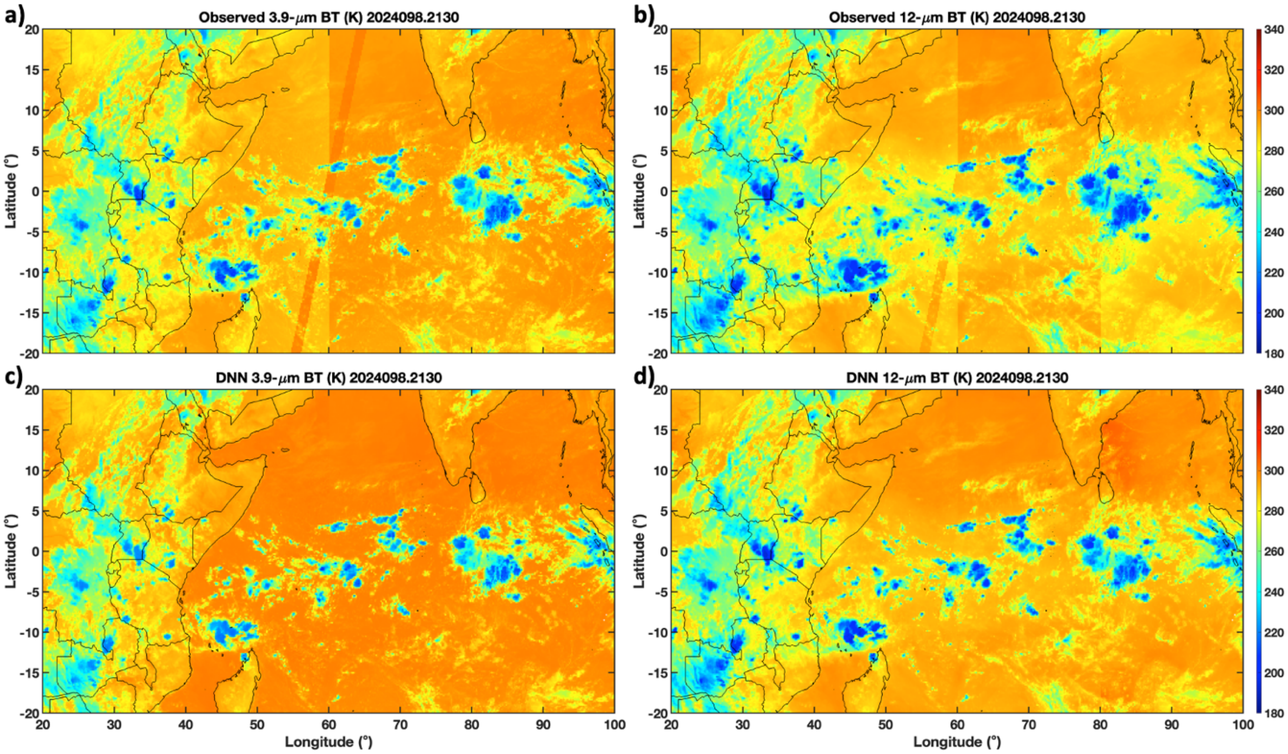

Figure 5. Same as Fig. 4 except focused on where the VIIRS swath crosses the MET10/MET9 boundary.

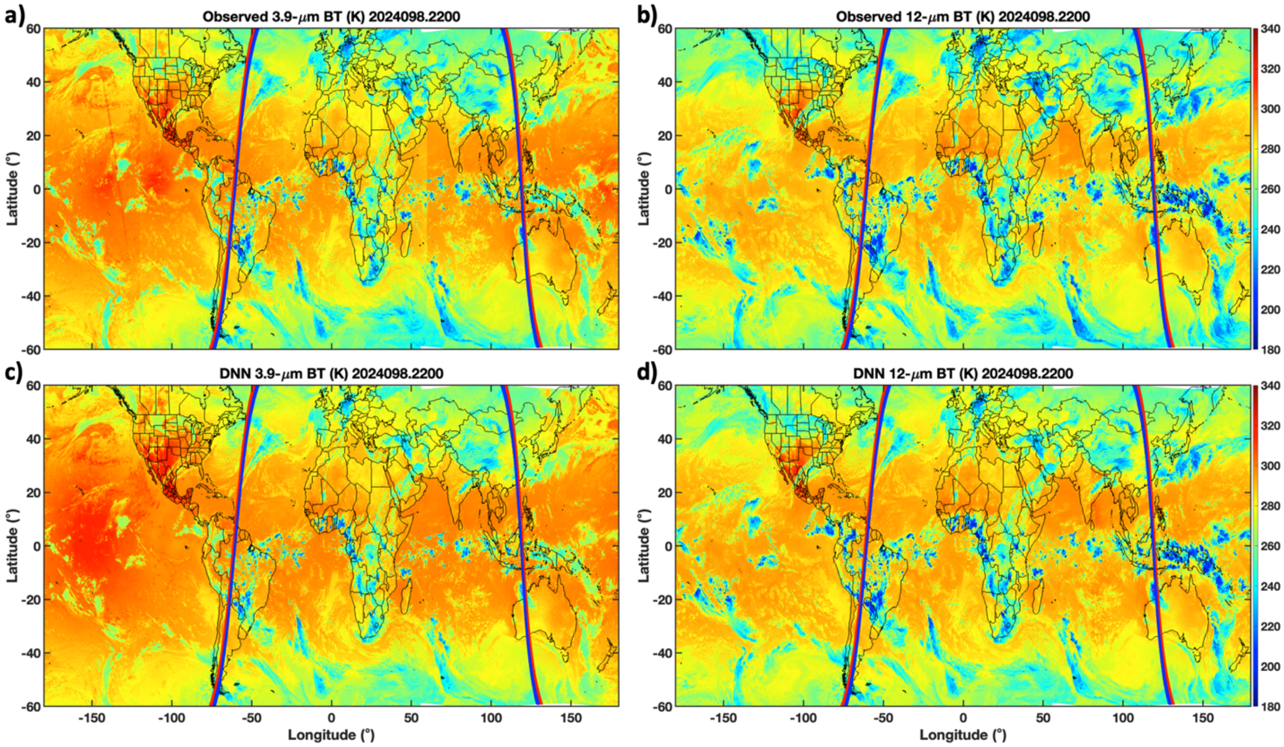

Figure 6. Same as Fig. 4, except at 22:00 UTC, demonstrating a daytime GEO and *at-nadir* VIIRS consistency evaluation, where the VIIRS swath extends roughly from 60º N, 150º W to 60º S, 120º W.

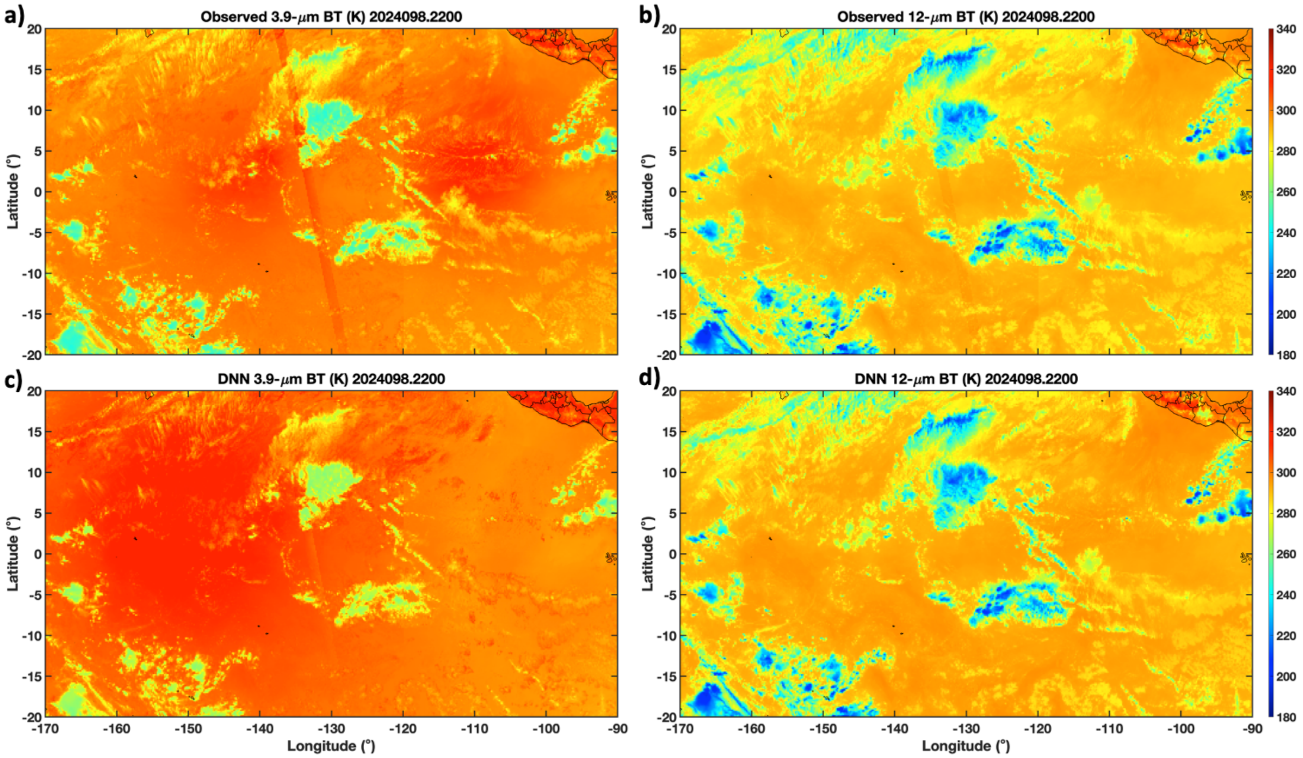

Figure 7. Same as Fig. 6 except focused on where the VIIRS swath crosses near the G18/G16 boundary.

easily viewable between roughly 10º N and 15º N, and 2) evidence of the VIIRS swath near the clouds at ~58º E and ~5º S – perhaps partly owed to uncertainty in the cloud height parallax correction. Regardless of these minor deficiencies, the DNN applications yield a much more seamless set of GEO-Ring radiances, with uncertainties quantified in Fig.1 and Table I.

Figures 6 and 7 are similar to Figs. 4 and 5, but occurring roughly 30 minutes later to allow for a daytime VIIRS consistency evaluation. In this case, the at-nadir VIIRS reference extends from roughly 60º N, 150º W to 60º S, 120º W. Again, Figs. 6 and 7 reveal improved seamlessness for both T39 and T12 at all GEO boundaries after the DNNs are applied. Also, as in the nighttime case, the VIIRS swath appears to have blended in with the GEO in Figs. 6c,d. The Fig. 7 enhanced view, however, reveals slightly more detail. The distinct VIIRS radiances are evident in T39 (Fig. 7a) and, to a lesser extent, T12 (Fig. 7b), and although the DNN effectively homogenized GEO T12 with at-nadir VIIRS T12 (Fig. 7d), evidence of the T39 VIIRS swath still persists in the form of slightly cooler BTs (Fig. 7c). The imperfect homogenization with the VIIRS T39 swath suggests inadequate characterization of the BRDF from the GEO angles. The RAA consideration looks particularly under-characterized given that there appears to be a small left-versus-right scan angle dependency in the VIIRS swath match, with seemingly better blending in the direction of the hot spot (Fig. 7c near 130º W and 0º N). Again, these results suggest there are caveats to consider if aiming to apply the *at-nadir* DNN approach for applications reliant on the daytime T39 radiances.

3.3 Cloud Algorithm Application

The effectiveness of the G16 and MET10 *ray-matched* DNNs in producing at-angle VIIRS-like BTs that preserve the GEO VZA considerations is demonstrated with a case study application of the G16 and modified MET10 Ed4 GEO cloud algorithms. The 10' grid-averaged daytime COD resulting from this application study are shown in Fig. 8, where Fig. 8a results are based on observed (unadjusted) T39, T87, T11, and T12 radiances and Fig. 8b results are based on *ray-matched* DNN VIIRS-like radiances. There is a notable improvement in the continuity of COD retrievals across the G16/MET10 boundary at 30º W when the DNN radiances are used (Fig. 8b). With the DNN radiances, the total variance and standard deviation of zonally averaged COD (averaged in log form) reduce by 14% and 25%, respectively. Note that the absolute accuracy of the cloud mask or COD is not being assessed here because, with the exception of the G16 side

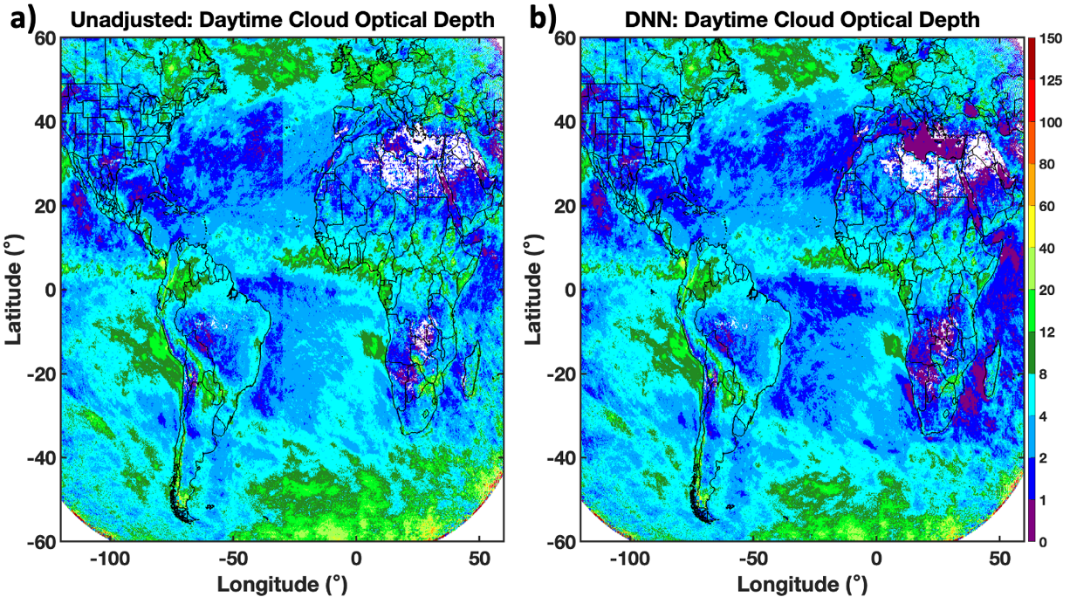

Figure 8. Daytime 10' grid average of COD (averaged in log form) from 21-31 July 2023 resulting from G16 and modified MET10 Ed4 GEO cloud algorithm processing based on a) observed and b) *ray-matched* DNN-estimated T39, T87, T11, and T12 radiances.

of the unadjusted radiances case (Fig. 8a), these results are not representative of a properly tuned cloud mask. That is, the point of this study is to assess the relative difference between results from two satellites that are using the same cloud masking assumptions for different input radiances, and therefore exact cloud occurrences and COD magnitudes are unimportant. Without a GEO cloud algorithm that is properly tuned to VIIRS-based expectations of atmospheric transmittance and cloud masking, we cannot yet make fair conclusions about the accuracy of the cloud mask or optical depth magnitudes. Nevertheless, the DNNs show promise in improving the relative consistency of GEO retrievals.

4. CONCLUSIONS

These proceedings highlight a novel machine-learning-based approach of tying GEO IR radiances, viewing geometry, and solar illumination geometry to a VIIRS reference, and thereby produce consistent GEO radiance measurements across the GEO-Ring. This DNN-driven IR homogenization approach accounts for the radiometric, spectral, and retrieval bias considerations of the imager calibration sequence. With multiple GEO IR channels as predictors for the coincident VIIRS reference, information about the spectral characteristics of the observed scene is inferred and mapped to VIIRS, which allows for more consistent IR channel radiances across GEO imagers. Through this method we can attain better-robust scene-dependent spectral band adjustments and limb darkening corrections than can be achieved with traditional techniques/models.

Two distinct DNN applications are developed, each with different advantage and purpose. In the *at-nadir* DNN, spectral biases and VZA dependencies are resolved, and continuous VIIRS-like radiances are achieved across all GEO domains. In the *ray-matched* DNN, only spectral biases are accounted for. Although the former produces a seamless GEO-Ring, the adjustment to *at-nadir* VIIRS means that estimated radiances skew toward an overhead-Sun BRDF feature, which accentuates the T39 hot spot. This feature may not be desirable for some applications that rely on daytime T39, and thus the *ray-matched* DNN may be more appropriate despite not yielding seamless GEO-Ring radiances. If otherwise accounting for limb darkening, e.g., as in the GEO Ed4 cloud algorithm, the *ray-matched* DNN can be an effective means of achieving a seamless global cloud assessment.

ACKNOWLEDGMENTS

This work was supported by the NASA Clouds and the Earth's Radiant Energy System (CERES) project. The authors thank Rabindra Palikonda for help with running the Ed4 GEO cloud algorithms.

REFERENCES

[1] Wielicki, B. A., Barkstrom, B. R., Harrison, E. F., Lee III, R. B., Smith, G. L., and Cooper, J. E., “Clouds and the Earth's Radiant Energy System (CERES): An Earth Observing System Experiment”, Bull. Amer. Meteor. Soc., Vol. 77, pp. 853–868 (1996).

[2] Doelling, D.R., D.F. Keyes, M.L. Nordeen, D. Morstad, C. Nguyen, B.A. Wielicki, D.F. Young, and M. Sun, “Geostationary enhanced temporal interpolation for CERES flux products”, J. Atmos. Oceanic Technol., Vol. 30 No. 6, pp. 1072–1090 (2013).

[3] Minnis, P., S. Sun-Mack, Y. Chen, F.-L. Chang, C. R. Yost, et al., “CERES MODIS Cloud Product Retrievals for Edition 4—Part I: Algorithm Changes”, IEEE T. Geosci. Remote Sens., Vol. 59, pp. 2744– 2780 (2020).

[4] Doelling, D. R., Haney, C., Bhatt, R., Scarino, B., and Gopalan, A., “Geostationary Visible Imager Calibration for the CERES SYN1deg Edition 4 Product”, Remote Sens., Vol. 10, 288 (2018).

[5] Doelling, D. R., Haney, C., Scarino, B. R., Gopalan, A., and Bhatt, R., “Improvements to the Geostationary Visible Imager Raymatching Calibration Algorithm for CERES Edition 4”, J. Atmos. Ocean. Tech., Vol. 33, pp. 2679–2698 (2016).

[6] Guo, Q., F. Chen, B. Chen, X. Feng, C. Yang, X. Wang, and Z. Zhang, “Internal-blackbody calibration (IBBC) approach and its operational application in FY-2 meteorological satellites”, Q. J. R. Meteorol. Soc. 142, pp. 3082–3096 (2016).

[7] Minnis, P., D. R. Doelling, D. F. Young, W. F. Miller, and D. P. Kratz, 2002, “Rapid calibration of operational and research meteorological satellite imagers. Part II: Comparison of infrared channels”, J. Atmos. Ocean. Tech., 19, pp. 1250–1266 (2002).

[8] Hewison, T. J., D. R. Doelling, C. Lukashin, D. Tobin, V. O. John, S. Joro, and B. Bojkov, “Extending the global space-based inter-calibration system (GSICS) to tie satellite radiances to an absolute scale.” Remote Sens. 12, 1782 (2020).

[9] Minnis, P., D. F. Young, and E. F. Harrison, “Examination of the relationship between outgoing infrared window and total longwave fluxes using satellite data”, J. Climate, 4, pp. 1114–1133 (1991).

[10] Katzoff, S. and G. L. Smith, “Effect of limb darkening on Earth radiation incident on a spherical satellite”, NASA Technical Note, Washington D. C. (1974).

[11] Minnis, P., A. V. Gambheer, and D. R. Doelling, “Azimuthal anisotropy of longwave and infrared window radiances from the Clouds and the Earth’s Radiant Energy System on the Tropical Rainfall Measuring Mission and Terra satellites”, J. Geophys. Res., 109, (2004).

[12] Kratz, D. P., “The correlated k-distribution technique as applied to the AVHRR channels”, J. Quant. Spectrosc. Radiat. Transfer, 53, pp. 501–507 (1995).

[13] Goody, R., R. West, L. Chen, and D. Crisp, “The correlated-k method for radiation calculations in nonhomogeneous atmospheres”, J. Quant. Spectrosc. Radiat. Transfer, 42, pp. 539–550 (1989).

[14] Salby, M. L., P. J. McBrid, and P. F. Callaghan, “Intersatellite Temperature Bias: Elimination through Statistical Calibration”, J. Atmos. Oceanic Technol., Vol. 25 No. 6, pp. 959–967 (2008).

[15] Scarino, B., D. R. Doelling, P. Minnis, A. Gopalan, T. Chee, R. Bhatt, C. Lukashin, and C. O. Haney, “A web-based tool for calculating spectral band difference adjustment factors derived from SCIAMACHY hyperspectral data”, IEEE Trans. Geosci. Rem. Sens., 54, pp. 2529–2542 (2016).

[16] Glorot, X., Bordes, A., and Bengio, Y., “Deep Sparse Rectifier Neural Networks”, J. of Mach. Learn. Re., Vo. 15, pp. 315–323 (2010).

[17] Bengio, Y., “Practical Recommendations for Gradient-based Training of Deep Architectures. Neural Networks: Tricks of the Trade”, Lecture Notes in Computer Science, Vol. 7700, G. Montavon, G. B. Orr, and K. R. Müller, Eds., Springer, Berlin, Heidelberg, pp. 437–374 (2012).

[18] LeCun Y., Bottou, L., Orr, G. B., and Müller, K. R., “Efficient BackProp. Neural Networks: Tricks of the Trade”, Lecture Notes in Computer Science, Vol. 1524, G. B. Orr, and K. R. Müller, Eds., Springer, Berlin, Heidelberg, pp. 9–50 (1998).

[19] Kingma, D. P. and Ba, J. L., “Adam: A Method for Stochastic Optimization”, Proc. ICLR (2015).

[20] Masters, D. and Luschi, C., “Revisiting Small Batch Training for Deep Neural Networks”, Graphcore Research, 18 pp. (2018).

[21] Prechelt, L., “Automatic Early Stopping Using Cross Validation: Quantifying the Criteria. Neural Networks, Vol. 11, pp. 761–767 (1998).